

The interaction between rising bubbles and cold fronts in cool core clusters

A. C. Fabian,¹* J. Zuhone,² and S. A. Walker,³

¹*Institute of Astronomy, Madingley Road, Cambridge CB3 0HA, UK*

²*Center for Astrophysics | Harvard & Smithsonian, Cambridge, MA 02138, USA*

³*Department of Physics and Astronomy, The University of Alabama in Huntsville, Huntsville, AL 35899, USA*

Accepted XXX. Received YYY; in original form ZZZ

ABSTRACT

We investigate whether the swirling cold front in the core of the Perseus Cluster of galaxies has affected the outer buoyant bubbles that originated from jets from the Active Galactic Nucleus in the central galaxy NGC1275. The inner bubbles and the Outer Southern bubble lie along a North-South axis through the nucleus, whereas the Outer Northern bubble appears rotated about 45 deg from that axis. Detailed numerical simulations of the interaction indicates that the Outer Northern bubble may have been pushed clockwise accounting for its current location. Given the common occurrence of cold fronts in cool core clusters, we raise the possibility that the lack of many clear outer bubbles in such environments may be due to their disruption by cold fronts.

Key words: keyword1 – keyword2 – keyword3

1 INTRODUCTION

The Perseus cluster of galaxies has proven to be an excellent demonstration of the action of Active Galactic Nucleus (AGN) Feedback in clusters, as well as a testbed for understanding the processes involved. A pair of inner cavities or bubbles on a North-South axis either side of the AGN in the central galaxy NGC1275 were first imaged in X-rays by ROSAT (Boehringer et al. 1993) and then studied in detail with Chandra (Fabian et al. 2000, 2003a, 2006). An outer bubble is seen further along the axis to the South with its partner lying to the North-West at an angle of about 45 deg from the axis of the inner bubbles. The axis of the inner bubbles is also marked to the North by optical H α filamentation, also seen faintly in soft X-rays, extending 50 kpc from the AGN (see Fig. 1).

Energy from the accreting black hole at the centre of NGC1275 powers jets seen at radio wavelengths as 3C84 (Pedlar et al. 1990; Gendron-Marsolais et al. 2020). The jets inflate the inner bubbles with plasma composed of relativistic particles and magnetic field which are buoyant in the denser ICM and rise to form a new set of outer bubbles. The power of the bubbling process of about $10^{44.5}$ to 10^{45} erg s⁻¹ is comparable to the energy loss of the cool core through radiating the X-ray emission we see. The whole bubbling process constitutes a dramatic example of AGN Feedback.

The off-axis arrangement of the NW bubble has in the past been considered to be due to precession of the central jets (Dunn et al. 2006; Falceta-Gonçalves et al. 2010; see also Sternberg & Soker 2008) or jet bending due to the bulk motion of the intracluster medium (ICM) relative to the AGN (Soker & Bisker 2006). Such effects would be expected to have influenced both of the outer bubbles but only the Northern one appears to be affected.

Here we consider the effects of the inner cold front that circles the centre of the cluster core. The front is due to sloshing motions

induced in the core by the close passage of a subcluster merger a few billion years ago. The NW outer bubble lies just inside the cold front where streaming motions occur that can carry the bubble in the required direction. An optical filament extends beyond the cold front to the N but then seems to twist also to the W. The S outer bubble has an unexplained double structure and lies beyond the cold front. We are of course viewing the system as projected on the plane of the Sky, whereas the jets that create the structure are oriented towards us in the N and away in the S. The inclination to the line of sight of the jets is a matter of debate and varies widely on which observations, from Radio (65 deg to line of sight) to Gamma-rays (23 deg) are being considered (see Hodgson et al. 2021). This uncertainty is due to which part of the inner jet system dominates the emission at different wavelengths and is a consequence of the dense clumpy central environment through which the jets initially propagate. The location of the most massive clumps could influence the final jet direction in a manner that is independent of the initial direction and so lead to the Northern Outer Bubble being offset from the Southern one. This would however require that the anisotropy lasts for the several Myr needed to form the bubbles, which is many dynamical times for the inner region and therefore unlikely.

Here we study the possible interaction between the Northern Outer Bubble and the Inner Cold Front. The Southern Bubble lies outside the cold front and we presume that the geometry is such that it did not directly interact with it. We do not aim for a perfect model but just illustrate using simulations that a twist in the direction of motion of a bubble of the amplitude seen is expected as it approaches and passes through a front.

2 BRIEF DESCRIPTION OF SLOSHING COLD FRONTS

Cold fronts are features in X-ray observations which are characterized by sharp surface brightness (SB) discontinuities in the ICM

* E-mail: acf@ast.cam.ac.uk

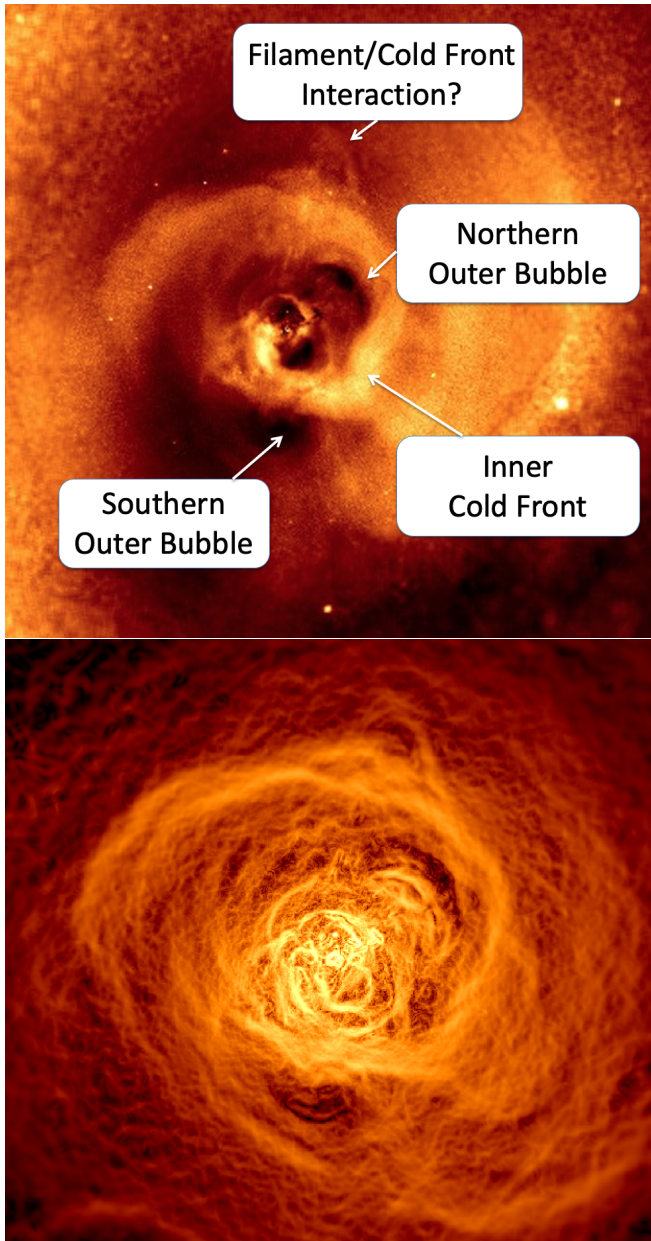


Figure 1. The core of the Perseus cluster imaged in X-rays by Chandra and displayed after application of (Top) an unsharp-mask and (Bottom) a Gaussian Gradient Method, which emphasises edges (from Walker et al. 2017). The upper image is about 400 kpc across and the lower is 200kpc. Salient features are labelled in the upper image and the next loop of the spiralling cold front is seen near the Western edge.

in which the measured temperature is colder on the brighter (and therefore denser) side of the feature. Simulations indicate that these features can be formed quite easily in mergers between galaxy clusters. This occurs when dense, low-entropy gas is brought into contact with more diffuse high-entropy gas and forms a contact discontinuity which travels at subsonic velocities. A recent review of cold fronts, including the details of the formation mechanisms in various circumstances, can be found in (ZuHone & Roediger 2016).

For a massive, cool-core cluster like Perseus, the cold fronts likely formed as a result of an off-center encounter with a subcluster. This process has been simulated in a number of works, including Ascasibar

& Markevitch (2006); ZuHone et al. (2010); Roediger et al. (2011, 2012). As the subcluster approaches the center of the larger cluster, it gravitationally accelerates both the gas and DM components of the core. However, the movement of the gas component is slowed by the ram pressure of the surrounding medium, and so it becomes spatially separated from the Dark Matter. After the subcluster has passed and its influence has weakened, the cold, low-entropy gas of the core falls back into the DM-dominated potential well, and begins to oscillate around it in a process dubbed “sloshing,” which produces cold fronts. Because the encounter with the subcluster was off-axis, it transfers angular momentum to the gas, and the sloshing gas motions and the cold fronts they produce are spiral-shaped. The cold fronts move radially outward slowly, with Mach number $\mathcal{M} \sim 0.1$, but the tangential flow underneath the front surface on the denser side is much faster, with $\mathcal{M} \sim 0.3 - 0.5$.

Figure 2 shows slices of the gas temperature for three different epochs in a simulation of gas sloshing that will be described in Section 3.1. The sharp gradients in temperature indicate the location of the cold fronts. Velocity vectors are overlaid, indicating that the flow pattern is largely tangential to the front surfaces and underneath them. As we show in Section 3.2, these tangential motions underneath the fronts can have significant effects on the evolution of cavities produced by the AGN at the core.

3 RESULTS

3.1 Simulation Methods

To carry out our simulations of gas sloshing combined with AGN jets, we use the AREPO code (Springel 2010), which employs a finite-volume Godunov method on an unstructured moving Voronoi mesh to evolve the equations of magnetohydrodynamics (MHD), and a Tree-PM solver to compute the self-gravity from gas and dark matter. The magnetic fields are evolved on the moving mesh using the Powell 8-wave scheme with divergence cleaning employed in (Pakmor & Springel 2013) and in the IllustrisTNG simulations (Marinacci et al. 2018). These simulations also include dark matter particles, which make up the bulk of the cluster’s mass and only interact with each other and the gas via gravity.

The simulations model a large, Perseus-like, cool-core cluster with $M \sim 10^{15} M_{\odot}$, with initial conditions taken from previous works (Ascasibar & Markevitch 2006; ZuHone et al. 2010, 2016, 2018, 2019, 2020). This cluster has an off-axis encounter with a DM-only subcluster of $M \sim 2 \times 10^{14} M_{\odot}$, which initiates sloshing motions which produce cold fronts. The ICM in the simulation has an initially tangled magnetic field with an initial plasma parameter $\beta = p_{\text{th}}/p_B = 100$. We use in this work the version of this simulation from ZuHone et al. (2020, hereafter Z20), with the same number of particles and cells, and mass and spatial resolution. The merger takes place within the $x - y$ plane, so that most (but not all) of the gas motions are in these directions. More details of the setup of this merger simulation are given in Section 2 of that paper.

We also use the same jet model as in Z20, originally presented in Weinberger et al. (2017). This method injects a bi-directional jet which is kinetically dominated, low density, and collimated. Kinetic, thermal, and magnetic energy is injected into two small spherical regions a few kpc from the location of a black hole particle. The material injected by the jet is marked by a passive tracer field ρ_{jet} and is advected along with the fluid for the rest of the simulation. In contrast to Z20, the material injected by the jet is composed of a 50/50 mixture of two fluids, one with $\gamma = 4/3$ representing cosmic rays (hereafter CRs) and another with $\gamma = 5/3$, the same as the ICM.

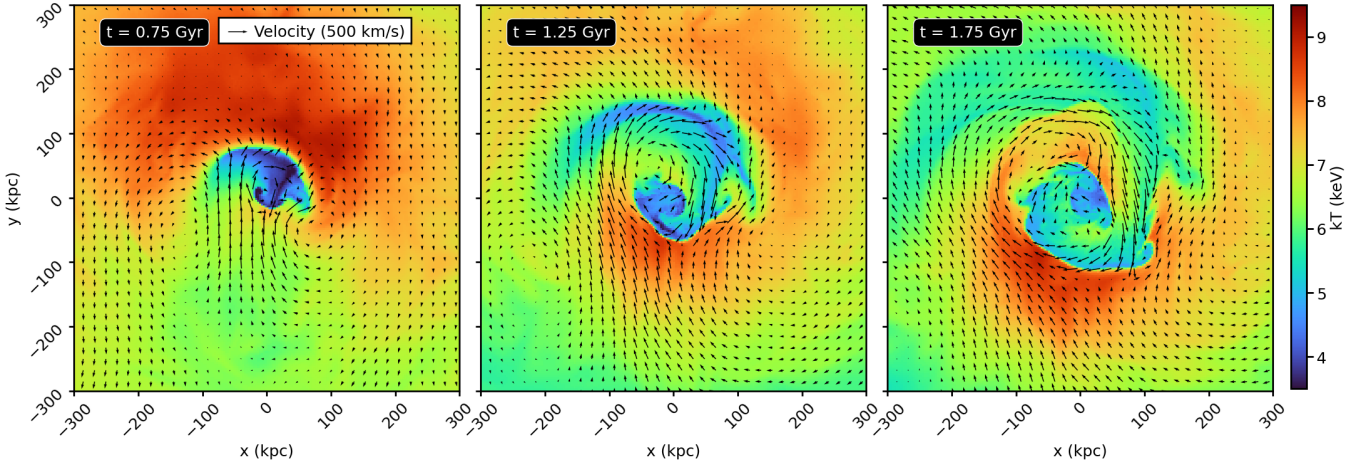


Figure 2. Slices through the gas temperature with velocity vectors overlaid for the three epochs of the merger simulation used in this work. Each slice is centered on the cluster potential minimum.

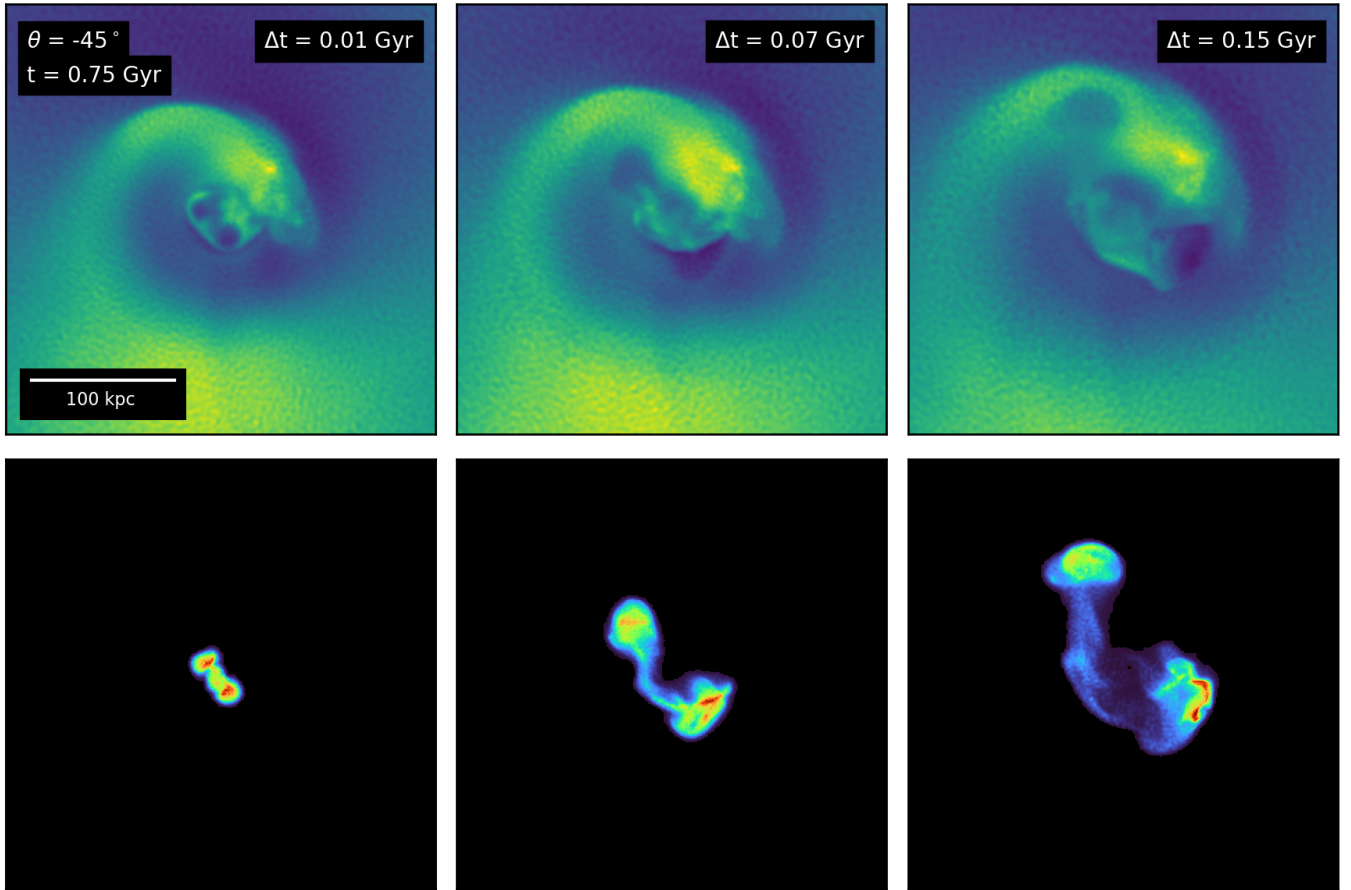


Figure 3. X-ray surface brightness residuals (top panels) and projected CR energy density (bottom panels) of our sloshing simulation where the jet was ignited at $t = 0.75$ Gyr at an angle of $\theta = -45^\circ$ from the x -axis, observed at three different epochs.

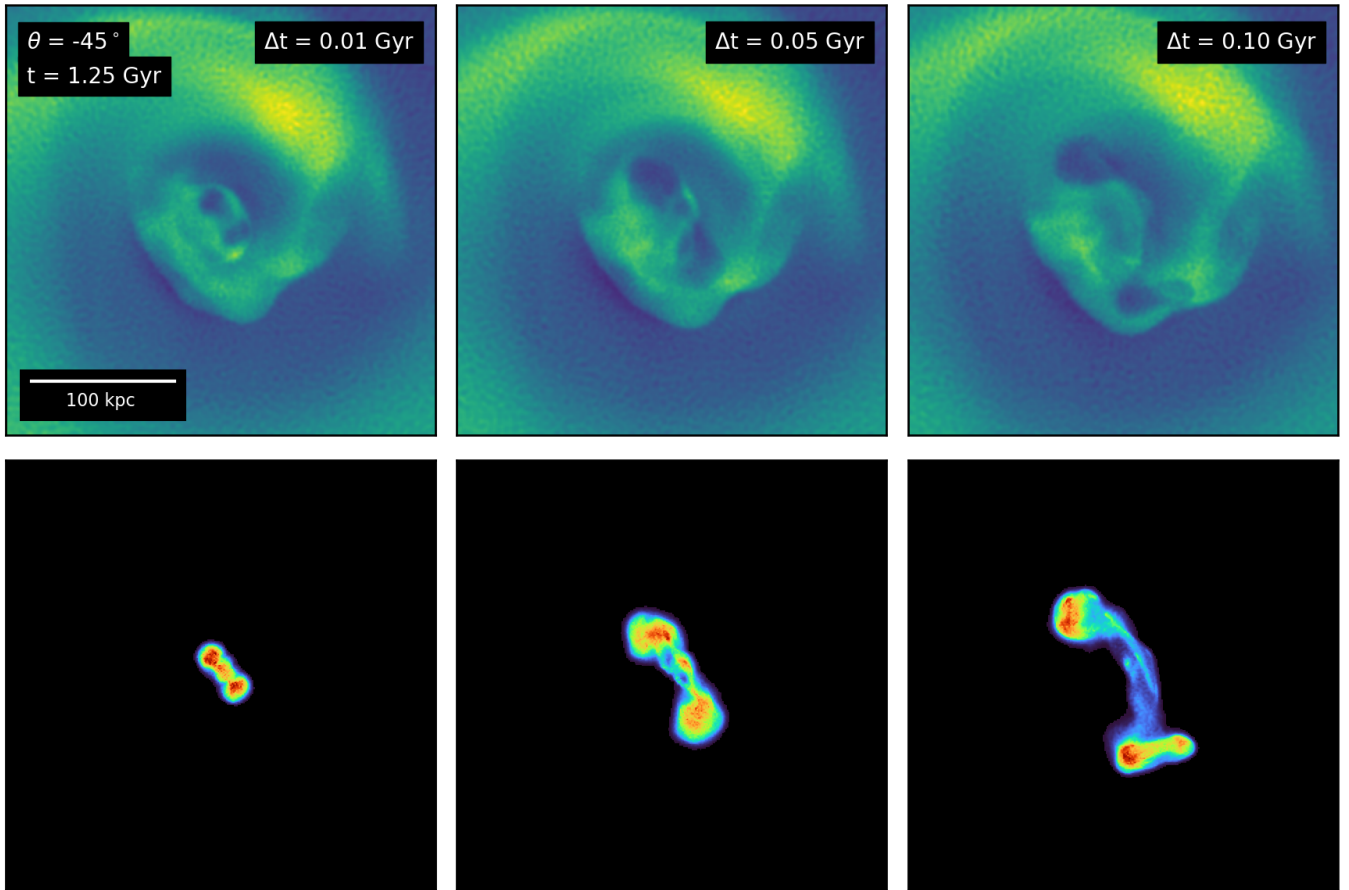


Figure 4. X-ray surface brightness residuals (top panels) and projected CR energy density (bottom panels) of our sloshing simulation where the jet was ignited at $t = 1.25$ Gyr at an angle of $\theta = -45^\circ$ from the x -axis, observed at three different epochs.

A black hole particle is placed at the cluster potential minimum, which serves as the site of the jet injection by the AGN. In each simulation, the jets are fired with a power $P_{\text{jet}} = 10^{45} \text{ erg s}^{-1}$ for a duration of $t_{\text{jet}} = 50$ Myr, so the resulting total energy injected is $E_{\text{jet}} \sim 1.6 \times 10^{60} \text{ erg}$ in each direction, which is a sum of kinetic, thermal, and magnetic energy. In the jet region, the magnetic and thermal pressures are equal ($\beta_{\text{jet}} = 1$), and the injected magnetic field is purely toroidal.

3.2 Simulation Results

We begin by choosing epochs of the merger simulation shortly after the subcluster passage but long enough for cold fronts to have developed. This ensures that the gas motions are fast and the first cold fronts to form have not yet propagated to a large radius. In reality, since structure formation is a continuous process, encounters with small subclusters may be frequent enough that new sloshing motions and cold fronts may be generated fairly frequently, so our choice of “favorable” epochs to affect the evolution of AGN bubbles is not arbitrary.

We examine three epochs, $t = 0.75, 1.25,$ and 1.75 Gyr, where the time is measured after the core passage of the subcluster (these are the three epochs shown in Figure 2). For each epoch, we perform several simulations, varying the jet orientation parameterized by the angle θ , defined as the angle measured counterclockwise from the

x -axis. We choose $\theta \in [-60^\circ, -45^\circ, -30^\circ, 0^\circ, 30^\circ, 45^\circ, 60^\circ, 90^\circ]$ (other orientations being degenerate with these due to the bipolar nature of the outflow).

Figures 3-5 shows the projected X-ray SB residuals and the projected CR energy density for a few representative cases from our simulations. The bubbles are visible in as cavities in the X-ray SB maps and as concentrations of CR energy density. Each case clearly shows that the bubbles begin along the jet axis, but as they rise they encounter the fast-moving ICM under the cold fronts and are subsequently blown off this axis. Fig. 3 shows rotation of the upper bubble similar to a similar degree seen in the Perseus cluster. Additionally, the gas motions stretch the bubbles in the tangential direction, producing pancake-shaped cavities. Both of these features of the cavities are seen in Perseus (Figure 1). The simulations suggest that the Southern bubble is unlikely to have escaped unscathed. The bending of the jets provided by the sloshing motions also produces features in the CR energy density maps that resemble wide-angle tails (WATs), which have already been shown to be easily produced in simulations by subsonic gas motions such as sloshing (Loken et al. 1995; Mendygral et al. 2012). We note that radiation losses on the most energetic electrons (spectral ageing) are responsible for the lack of detectable radio emission at 1 GHz from the cosmic rays in the outer bubbles of Perseus.

For completeness, we also show similar maps of all jet orientations for all three epochs in Appendix A. These plots show other interesting

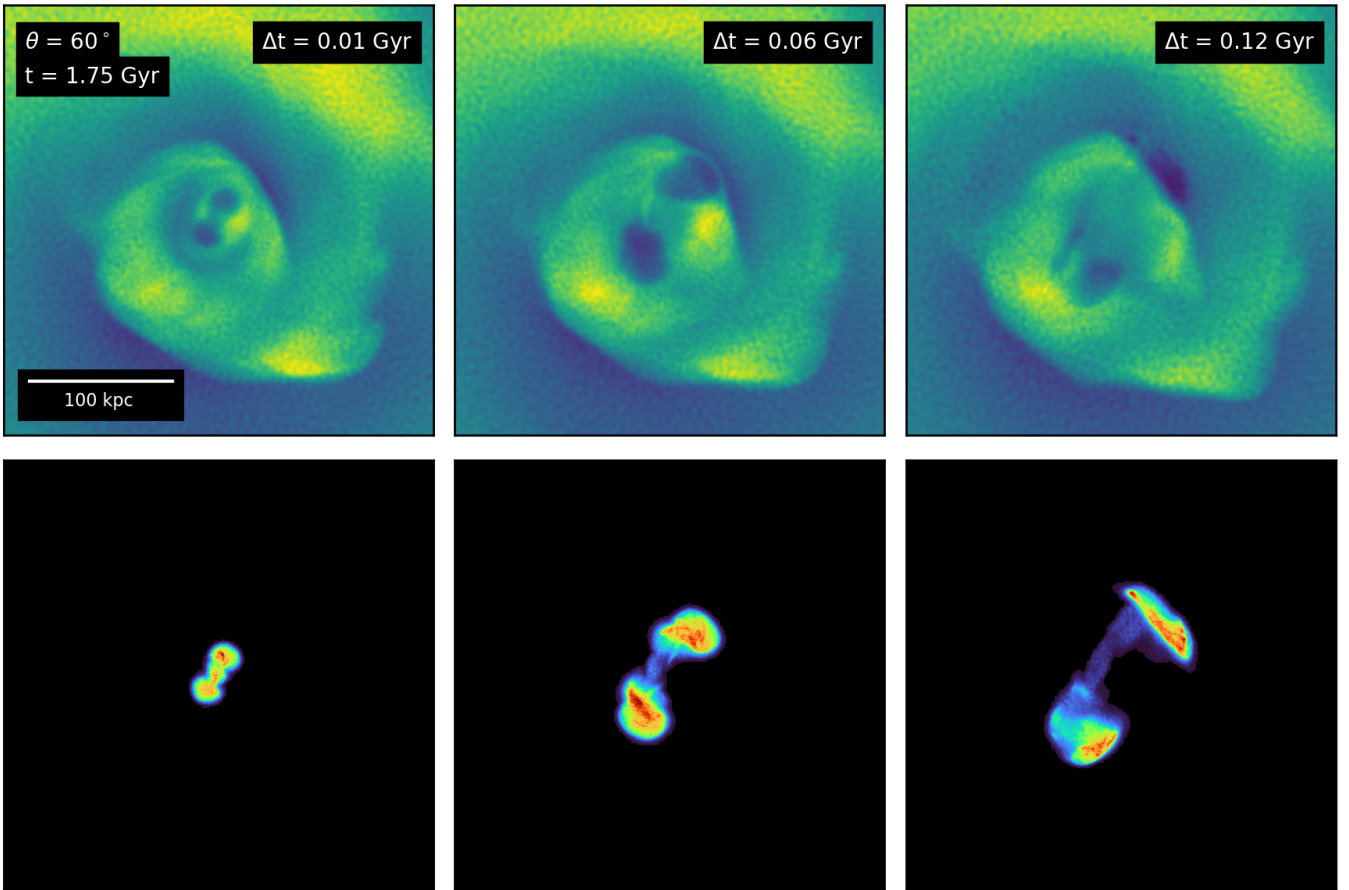


Figure 5. X-ray surface brightness residuals (top panels) and projected CR energy density (bottom panels) of our sloshing simulation where the jet was ignited at $t = 1.75$ Gyr at an angle of $\theta = 60^\circ$ from the x -axis, observed at three different epochs.

features depending on the orientation, including bubbles which split into two, resulting in three observed cavities, and WATs of various shapes at late stages.

4 DISCUSSION

We have shown that interactions between outer bubbles and a sloshing cold front can deflect the trajectories of the bubbles and cause their positions to depart from the line of their initial trajectory. Also, passage through a cold front can seriously distort and possibly destroy a bubble. With that in mind we have searched the literature for evidence of multiple bubbles. Large compilations of bubbles (or X-ray cavities) appear in [Diehl et al. \(2008\)](#) and [Birzan et al. \(2020\)](#), and there are many reports on individual sources. One striking result is that multiple pairs of bubbles in the same system are rare.

Clear examples are found in some groups of galaxies, such as NGC 5813 ([Randall et al. 2011, 2015](#)) and NGC 5044 ([Schellenberger et al. 2021](#)). The bubbles are smaller than those in clusters and groups tend not to have cold fronts, contrary to the cool cores of rich clusters where perhaps two-thirds have cold fronts ([Ghizzardi et al. 2010](#); [ZuHone et al. 2016](#)). Hydra-A has multiple sets of relatively large bubbles at the centre of a cluster ([Wise et al. 2007](#)) which does not appear to host a cold front but a very large shock front at a radius of 200–300 kpc ([Nulsen et al. 2005](#)). A precessing jet model for the Hydra-A jets has been presented by [Nawaz et al. \(2016\)](#). As

mentioned above, most cool-core clusters with bubbles show just one pair¹. It is of course possible that outer bubbles are present but undetectable due to reasons of contrast or lower surface brightness (see [Panagoulia et al. 2014](#) for a discussion of bubble detectability in nearby systems), but none are seen even in objects with deep X-ray images.

A more likely explanation from the present work is that buoyant outer bubbles may be sufficiently distorted or destroyed by interacting with cold fronts. This would mean that the effects like the interaction seen in the Perseus Cluster may be common. For example, [Sanders et al. \(2009\)](#) presented results on the cluster 2A 0335+096, which shows evidence of both sloshing cold fronts and 4 X-ray cavities which may have been transported tangentially by the sloshing motions or even split apart by them (see the $\theta = 45^\circ$, $\Delta t = 0.1$ Gyr panel of Figures A5 and A6 for examples from our simulations in the Appendix).

One feature that we defer to later work is possible interactions between the $H\alpha$ filaments of the Perseus Cluster and the sloshing cold fronts. The filaments contain both atomic and molecular gas ([Hatch et al. 2005](#); [Salomé et al. 2006](#); [Lim et al. 2012](#)). The NW outer bubble in the Perseus Cluster does have a "horseshoe" filament

¹ The nearby M87 system shows several small bubbles adjacent to the E inner bubble ([Forman et al. 2007](#)). These are unlikely to be related to the interactions discussed here.

below it (Conselice et al. 2001; Fabian et al. 2003b) which may reveal the fluid flow. The interaction of dense filaments with the swirling lighter gas is not straightforward and will depend on the magnetic coupling between the two media.

There are a number of areas for future work. Our simulated cluster, while a close match to Perseus in terms of mass, temperature, and shapes of the cold fronts, is not an exact match, especially with respect to the effects of AGN feedback. In subsequent works, we will attempt to simulate a closer match to the Perseus Cluster, reproducing the sizes and orientation of the cold fronts and cavities, as well as the properties of the velocity field already observed by *Hitomi* (Hitomi Collaboration et al. 2016). Indeed the highest velocity sector reported from the analysis by (Hitomi Collaboration et al. 2018) is the one covering the Northern Outer Bubble and neighbouring cold front, the site of the interaction at the heart of this paper. Velocity fields in the cores of the Perseus and Virgo clusters have been obtained at lower spectral resolution with *XMM-Newton* by (Sanders et al. 2020; Gatuzz et al. 2021, submitted). In the near future *XRISM* (Tashiro et al. 2018) will have a detector similar to that on *Hitomi* (with a resolution of 5 eV) and in the early 2030s *Athena* (Barcons et al. 2017) will observe clusters with yet higher spectral resolution (2.5 eV) and good spatial resolution (about 6 arcsec). A deeper *Chandra* image of the Perseus cluster would reveal the interaction and properties of the outer bubbles and inner cold front in greater detail.

In summary, the offset location of the Outer Northern Bubble in the Perseus Cluster suggests that a strong interaction is taking place with the Inner Cold Front. Our simulations coupled with the lack of multiple bubble systems in rich clusters imply that cold fronts disrupt outer bubbles.

ACKNOWLEDGEMENTS

JAZ acknowledges support from the *Chandra* X-ray Center, which is operated by the Smithsonian Astrophysical Observatory for and on behalf of NASA under contract NAS8-03060. The simulations were performed on the “Pleiades” high-performance computing system at the NASA Advanced Supercomputing facility at NASA/Ames Research Center.

DATA AVAILABILITY

The *Chandra* data used in the paper are publicly available from the *Chandra* Data Archive (CDA). FITS images from the simulation data will be made available on the Galaxy Cluster Merger Catalog at <http://gcmc.hub.yt>.

REFERENCES

- Ascasibar Y., Markevitch M., 2006, *ApJ*, **650**, 102
 Barcons X., et al., 2017, *Astronomische Nachrichten*, **338**, 153
 Birzan L., et al., 2020, *MNRAS*, **496**, 2613
 Böhringer H., Voges W., Fabian A. C., Edge A. C., Neumann D. M., 1993, *MNRAS*, **264**, L25
 Conselice C. J., Gallagher John S. I., Wyse R. F. G., 2001, *AJ*, **122**, 2281
 Diehl S., Li H., Fryer C. L., Rafferty D., 2008, *ApJ*, **687**, 173
 Dunn R. J. H., Fabian A. C., Sanders J. S., 2006, *MNRAS*, **366**, 758
 Fabian A. C., et al., 2000, *MNRAS*, **318**, L65
 Fabian A. C., Sanders J. S., Allen S. W., Crawford C. S., Iwasawa K., Johnstone R. M., Schmidt R. W., Taylor G. B., 2003a, *MNRAS*, **344**, L43
 Fabian A. C., Sanders J. S., Crawford C. S., Conselice C. J., Gallagher J. S., Wyse R. F. G., 2003b, *MNRAS*, **344**, L48

- Fabian A. C., Sanders J. S., Taylor G. B., Allen S. W., Crawford C. S., Johnstone R. M., Iwasawa K., 2006, *MNRAS*, **366**, 417
 Falcata-Gonçalves D., Caproni A., Abraham Z., Teixeira D. M., de Gouveia Dal Pino E. M., 2010, *ApJ*, **713**, L74
 Forman W., et al., 2007, *ApJ*, **665**, 1057
 Gendron-Marsolais M., et al., 2020, *MNRAS*, **499**, 5791
 Ghizzardi S., Rossetti M., Molendi S., 2010, *A&A*, **516**, A32
 Hatch N. A., Crawford C. S., Fabian A. C., Johnstone R. M., 2005, *MNRAS*, **358**, 765
 Hitomi Collaboration Aharonian F., Akamatsu H., Akimoto F., Allen S. W., Anabuki N., Angelini L., et al. 2016, *Nature*, **535**, 117
 Hitomi Collaboration et al., 2018, *PASJ*, **70**, 9
 Hodgson J. A., et al., 2021, arXiv e-prints, p. arXiv:2104.03081
 Lim J., Ohya Y., Chi-Hung Y., Dinh-V-Trung Shiang-Yu W., 2012, *ApJ*, **744**, 112
 Loken C., Roettiger K., Burns J. O., Norman M., 1995, *ApJ*, **445**, 80
 Marinacci F., et al., 2018, *MNRAS*, **480**, 5113
 Mendygral P. J., Jones T. W., Dolag K., 2012, *ApJ*, **750**, 166
 Nawaz M. A., Bicknell G. V., Wagner A. Y., Sutherland R. S., McNamara B. R., 2016, *MNRAS*, **458**, 802
 Nulsen P. E. J., McNamara B. R., Wise M. W., David L. P., 2005, *ApJ*, **628**, 629
 Pakmor R., Springel V., 2013, *MNRAS*, **432**, 176
 Panagoulia E. K., Fabian A. C., Sanders J. S., Hlavacek-Larrondo J., 2014, *MNRAS*, **444**, 1236
 Pedlar A., Ghataure H. S., Davies R. D., Harrison B. A., Perley R., Crane P. C., Unger S. W., 1990, *MNRAS*, **246**, 477
 Randall S. W., et al., 2011, *ApJ*, **726**, 86
 Randall S. W., et al., 2015, *ApJ*, **805**, 112
 Roediger E., Brüggem M., Simionescu A., Böhringer H., Churazov E., Forman W. R., 2011, *Mon. Not. R. Astron. Soc.*, **413**, 2057
 Roediger E., Lovisari L., Dupke R., Ghizzardi S., Brüggem M., Kraft R. P., Machacek M. E., 2012, *Mon. Not. R. Astron. Soc.*, **420**, 3632
 Salomé P., et al., 2006, *A&A*, **454**, 437
 Sanders J. S., Fabian A. C., Taylor G. B., 2009, *MNRAS*, **396**, 1449
 Sanders J. S., et al., 2020, *A&A*, **633**, A42
 Schellenberger G., David L. P., Vrtiljek J., O’Sullivan E., Giacintucci S., Forman W., Jones C., Venturi T., 2021, *ApJ*, **906**, 16
 Soker N., Bisker G., 2006, *MNRAS*, **369**, 1115
 Springel V., 2010, *MNRAS*, **401**, 791
 Sternberg A., Soker N., 2008, *MNRAS*, **384**, 1327
 Tashiro M., Maejima H., Toda K., Kelley R., Reichenthal L., Lobell J., Petre R., et al. 2018, in den Herder J.-W. A., Nikzad S., Nakazawa K., eds, Society of Photo-Optical Instrumentation Engineers (SPIE) Conference Series Vol. 10699, Space Telescopes and Instrumentation 2018: Ultraviolet to Gamma Ray, p. 1069922, doi:10.1117/12.2309455
 Walker S. A., Hlavacek-Larrondo J., Gendron-Marsolais M., Fabian A. C., Intema H., Sanders J. S., Bamford J. T., van Weeren R., 2017, *MNRAS*, **468**, 2506
 Weinberger R., Ehlert K., Pfrommer C., Pakmor R., Springel V., 2017, *MNRAS*, **470**, 4530
 Wise M. W., McNamara B. R., Nulsen P. E. J., Houck J. C., David L. P., 2007, *ApJ*, **659**, 1153
 ZuHone J. A., Roediger E., 2016, *Journal of Plasma Physics*, **82**, 535820301
 ZuHone J. A., Markevitch M., Johnson R. E., 2010, *ApJ*, **717**, 908
 ZuHone J. A., Miller E. D., Simionescu A., Bautz M. W., 2016, *ApJ*, **821**, 6
 ZuHone J. A., Miller E. D., Bulbul E., Zhuravleva I., 2018, *ApJ*, **853**, 180
 ZuHone J. A., Zavala J., Vogelsberger M., 2019, *ApJ*, **882**, 119
 ZuHone J. A., Markevitch M., Weinberger R., Nulsen P., Ehlert K., 2020, arXiv e-prints, p. arXiv:2012.02001

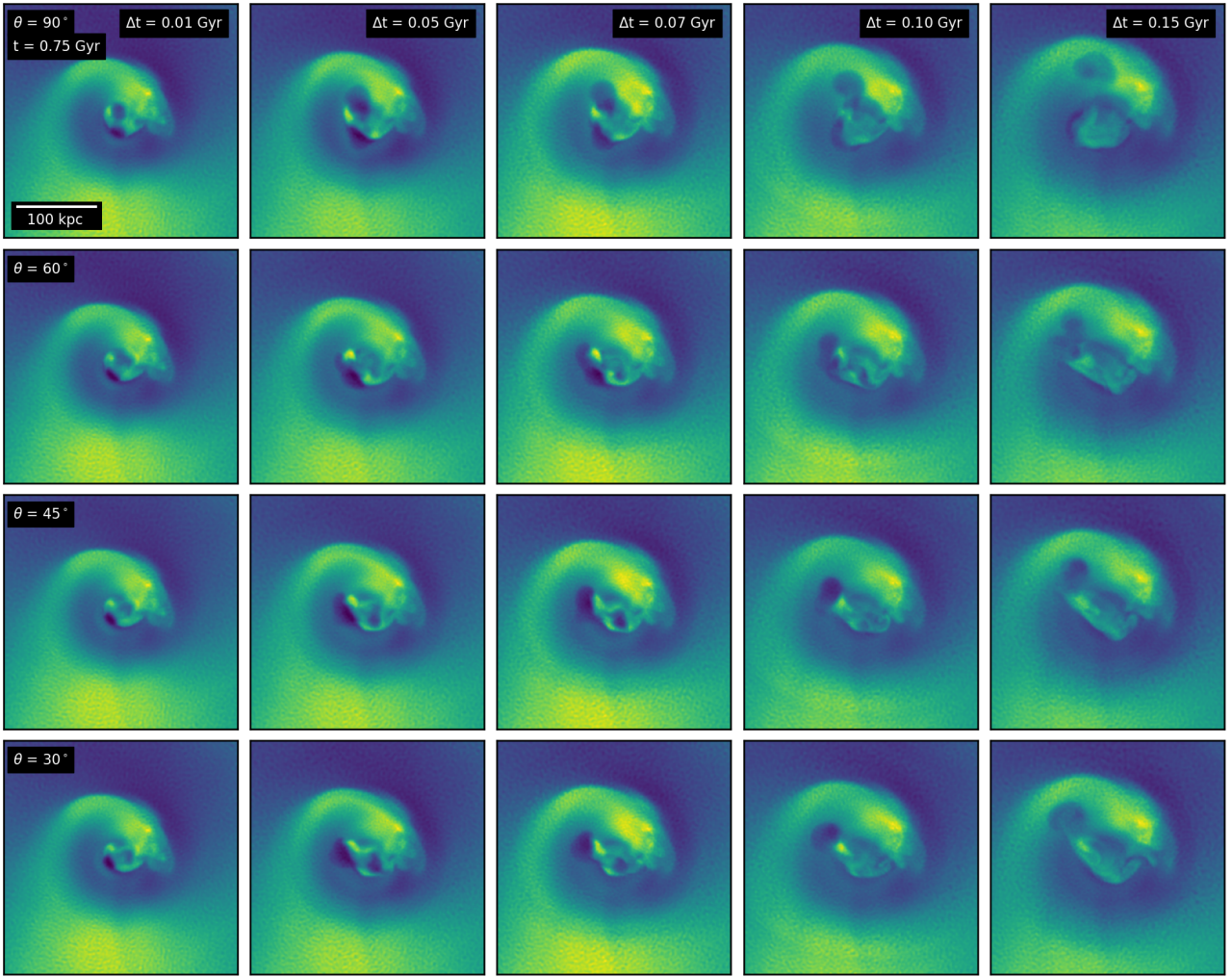


Figure A1. X-ray surface brightness residuals of simulation with sloshing gas motions and AGN jets, where the jet axis is 90, 60, 45, and 30 degrees from the horizontal. Epochs shown are 0.01, 0.05, 0.07, 0.1, and 0.15 Gyr from the jet ignition.

APPENDIX A: SUPPLEMENTAL X-RAY SURFACE BRIGHTNESS AND COSMIC RAY ENERGY DENSITY MAPS

This paper has been typeset from a $\text{\TeX}/\text{\LaTeX}$ file prepared by the author.

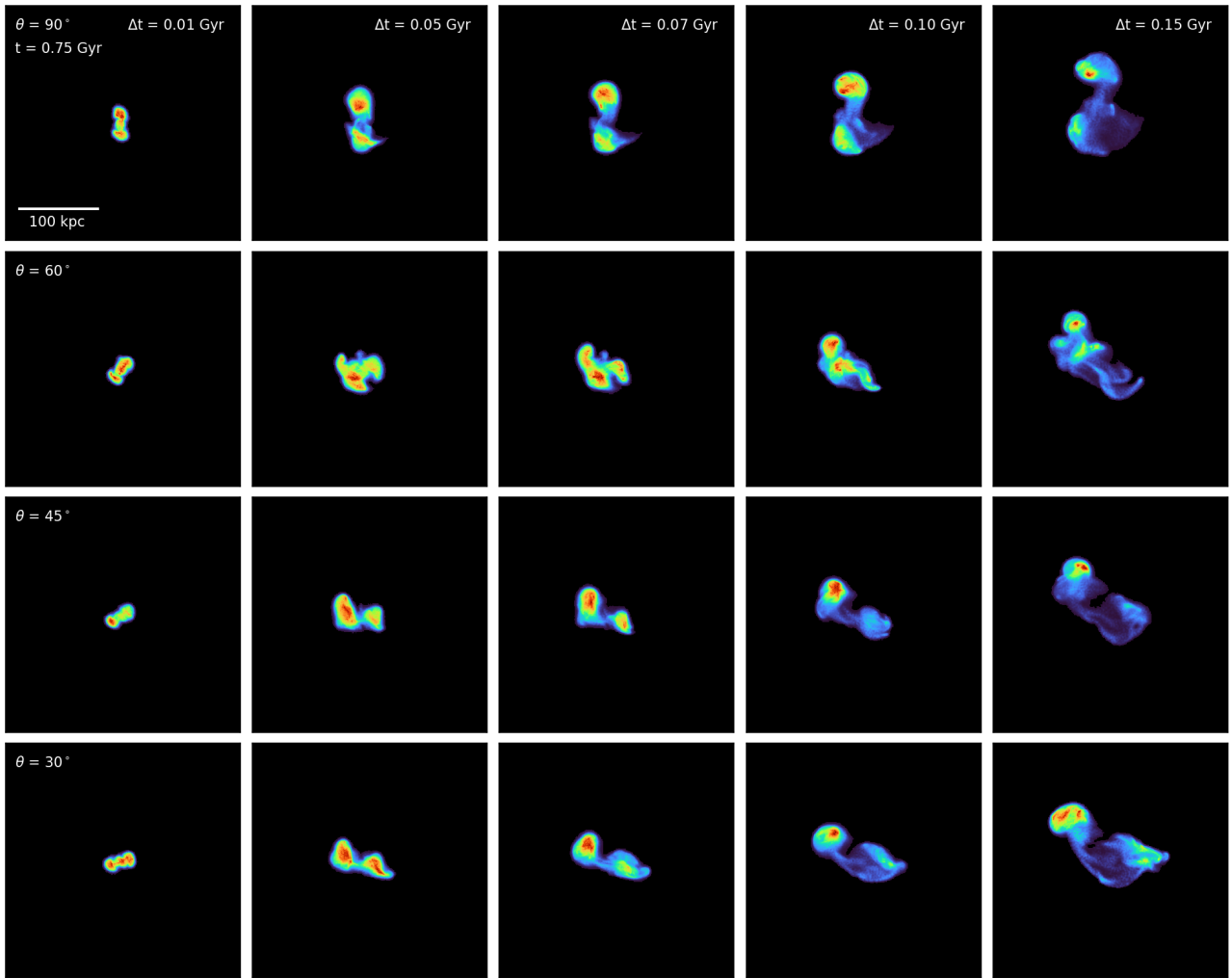


Figure A2. Projected CR energy density of simulation with sloshing gas motions and AGN jets, where the jet axis is 90, 60, 45, and 30 degrees from the horizontal. Epochs shown are $\Delta t = 0.01, 0.05, 0.07, 0.1,$ and 0.15 Gyr from the jet ignition at $t = 0.75$ Gyr.

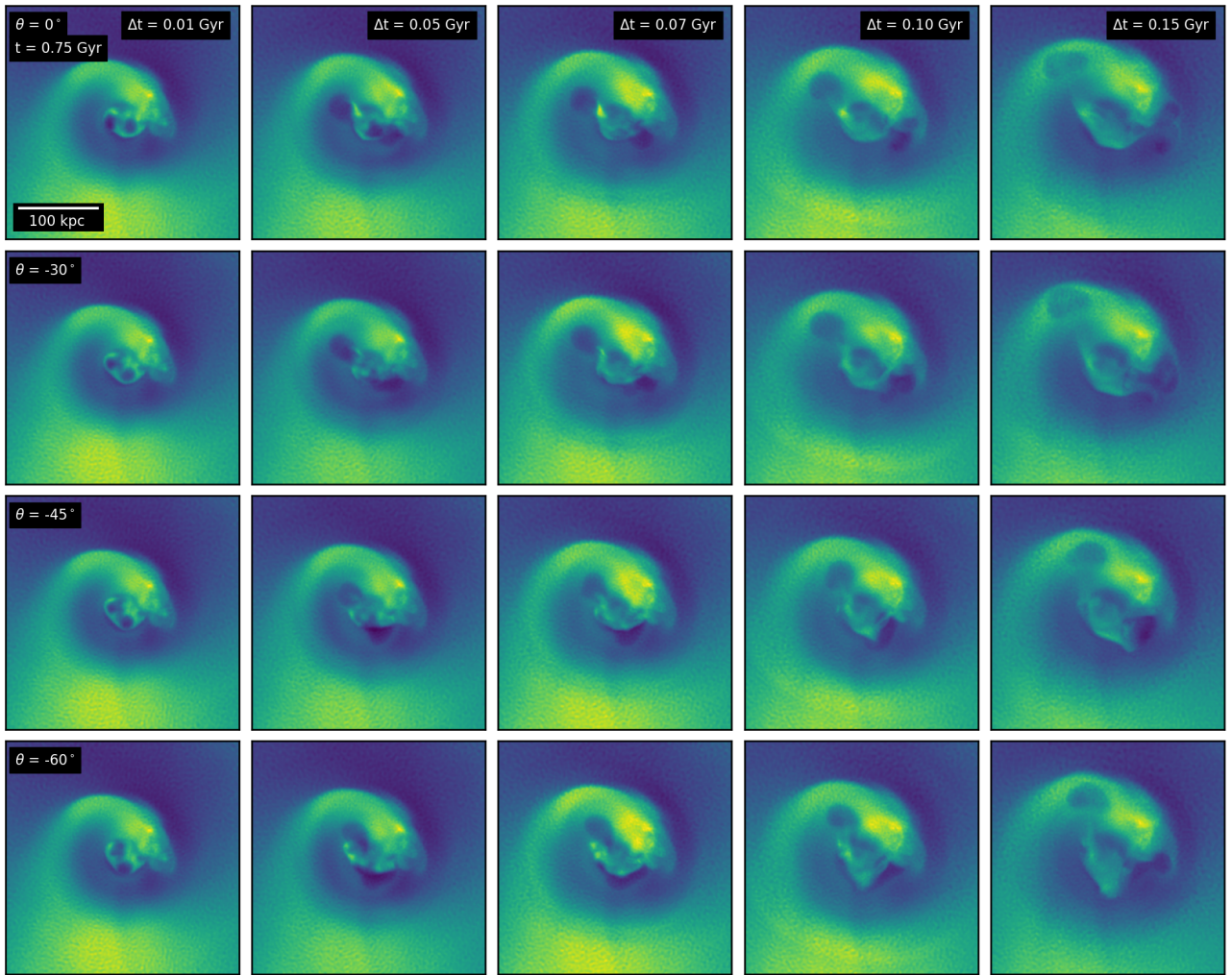


Figure A3. X-ray surface brightness residuals of simulation with sloshing gas motions and AGN jets, where the jet axis is 0, -30, -45, and -60 degrees from the horizontal. Epochs shown are $\Delta t = 0.01, 0.05, 0.07, 0.1,$ and 0.15 Gyr from the jet ignition at $t = 0.75$ Gyr.

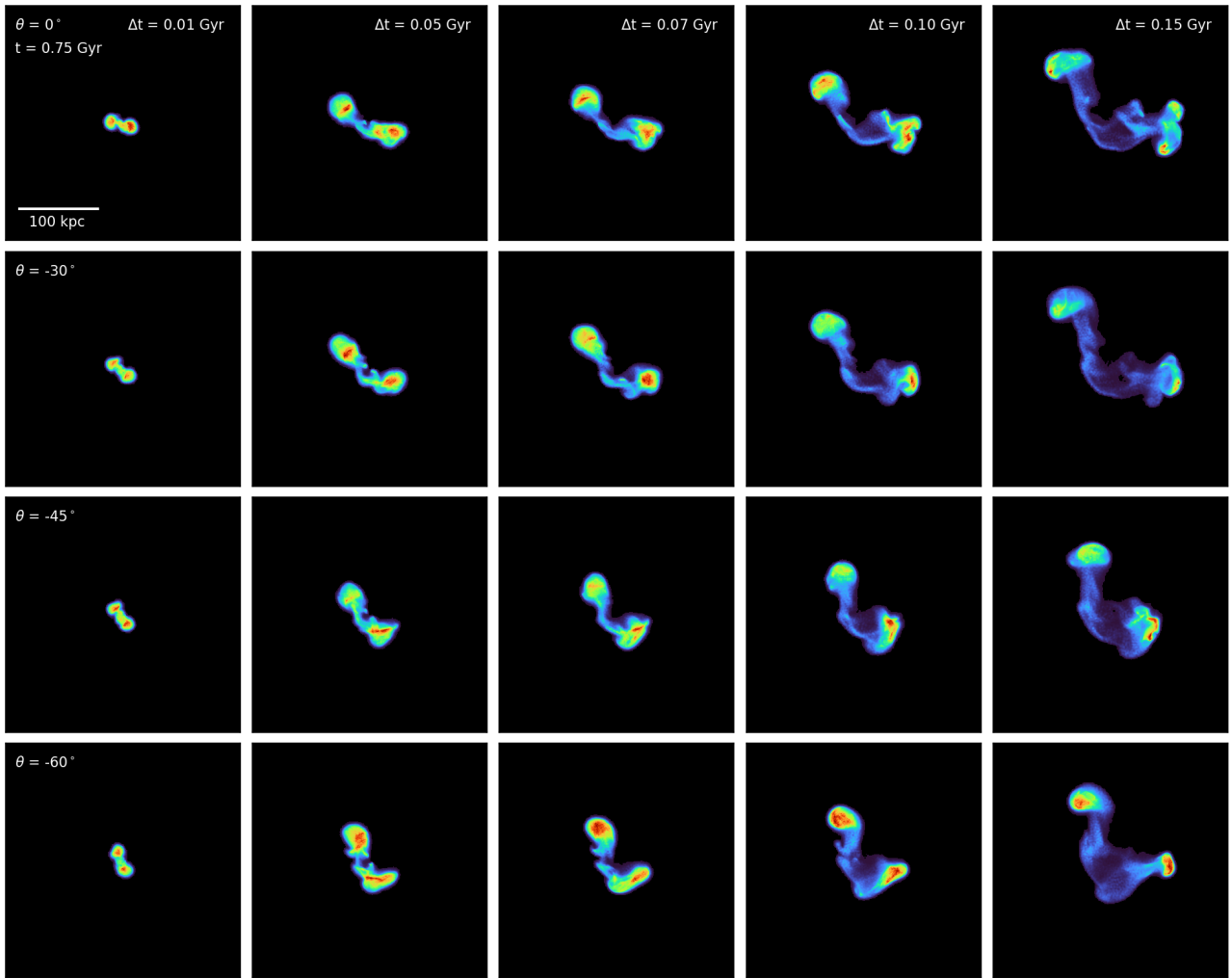


Figure A4. Projected CR energy density of simulation with sloshing gas motions and AGN jets, where the jet axis is 0, -30, -45, and -60 degrees from the horizontal. Epochs shown are $\Delta t = 0.01, 0.05, 0.07, 0.1,$ and 0.15 Gyr from the jet ignition at $t = 0.75$ Gyr.

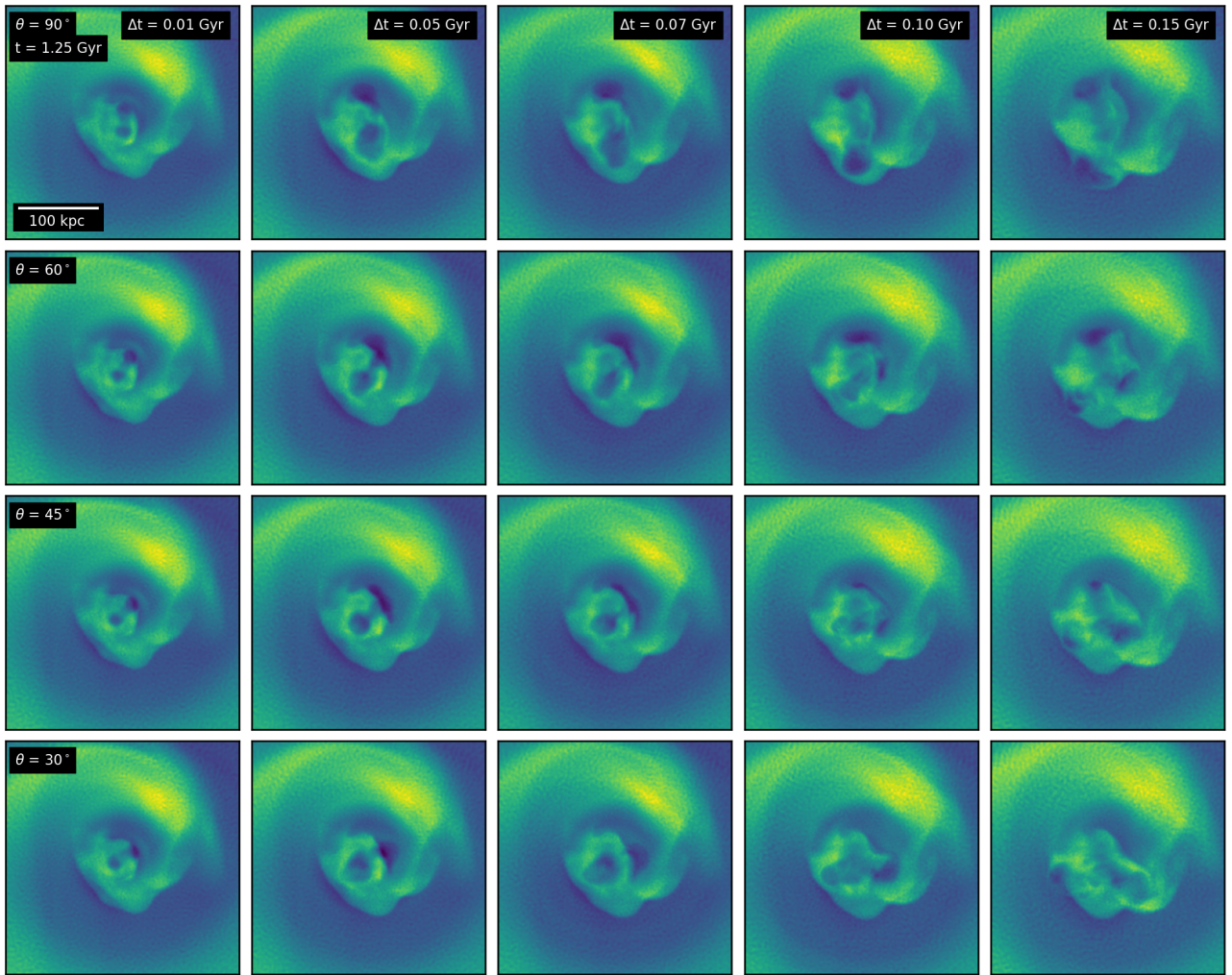


Figure A5. X-ray surface brightness residuals of simulation with sloshing gas motions and AGN jets, where the jet axis is 90, 60, 45, and 30 degrees from the horizontal. Epochs shown are $\Delta t = 0.01, 0.05, 0.07, 0.1,$ and 0.15 Gyr from the jet ignition at $t = 1.25$ Gyr.

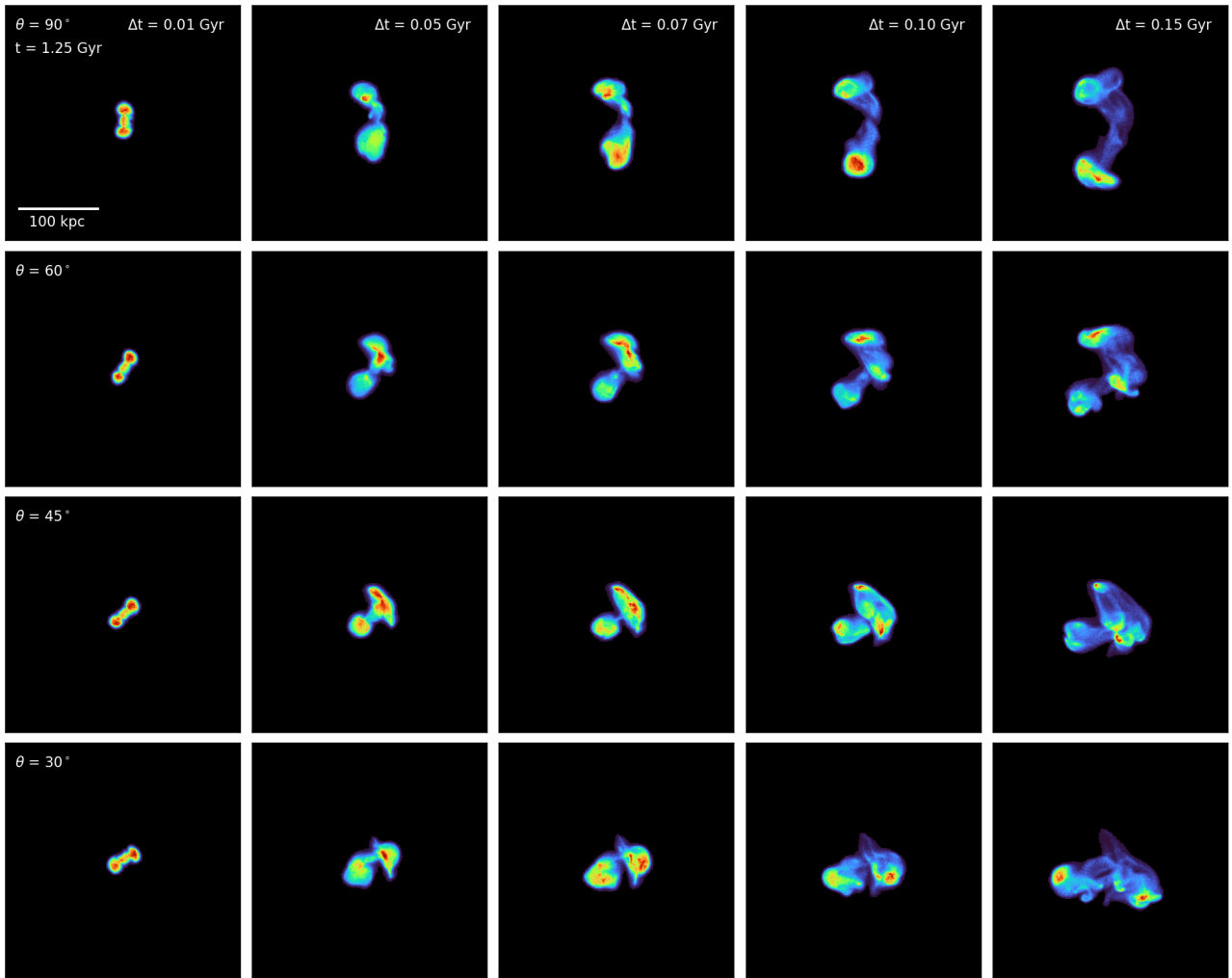


Figure A6. Projected CR energy density of simulation with sloshing gas motions and AGN jets, where the jet axis is 90, 60, 45, and 30 degrees from the horizontal. Epochs shown are $\Delta t = 0.01, 0.05, 0.07, 0.1,$ and 0.15 Gyr from the jet ignition at $t = 1.25$ Gyr.

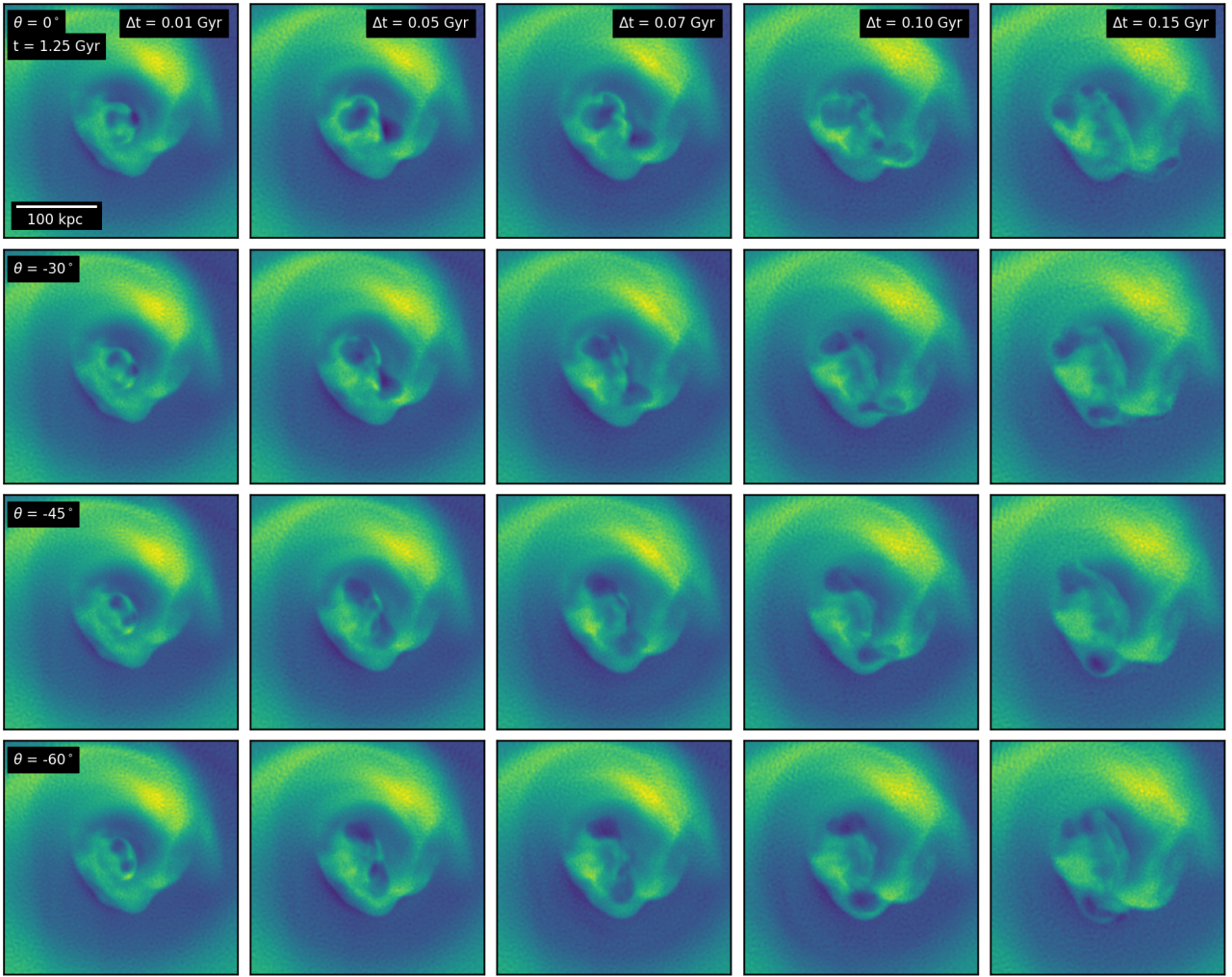


Figure A7. X-ray surface brightness residuals of simulation with sloshing gas motions and AGN jets, where the jet axis is 0, -30, -45, and -60 degrees from the horizontal. Epochs shown are $\Delta t = 0.01, 0.05, 0.07, 0.1,$ and 0.15 Gyr from the jet ignition at $t = 1.25$ Gyr.

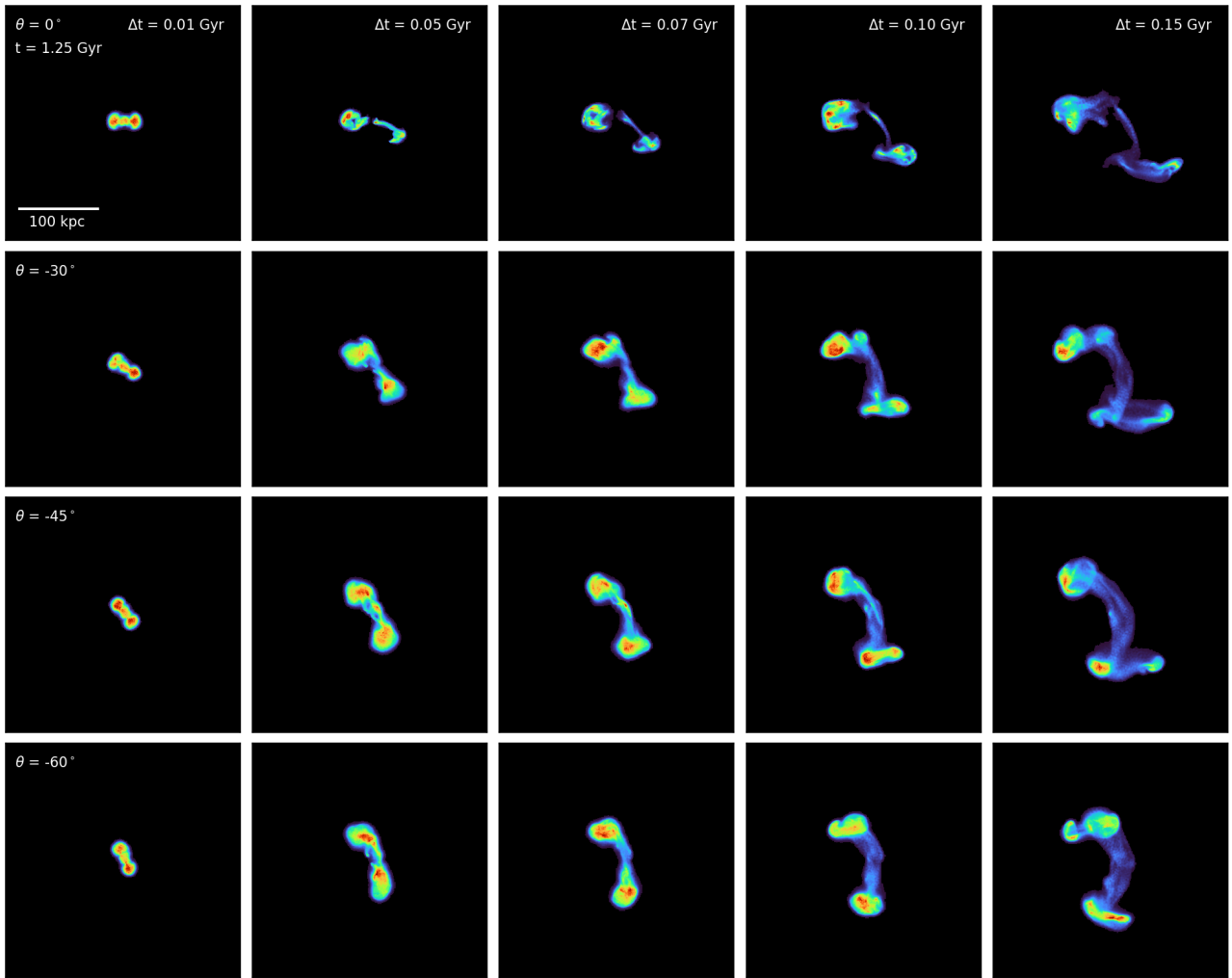


Figure A8. Projected CR energy density of simulation with sloshing gas motions and AGN jets, where the jet axis is 0, -30, -45, and -60 degrees from the horizontal. Epochs shown are $\Delta t = 0.01, 0.05, 0.07, 0.1,$ and 0.15 Gyr from the jet ignition at $t = 1.25$ Gyr.

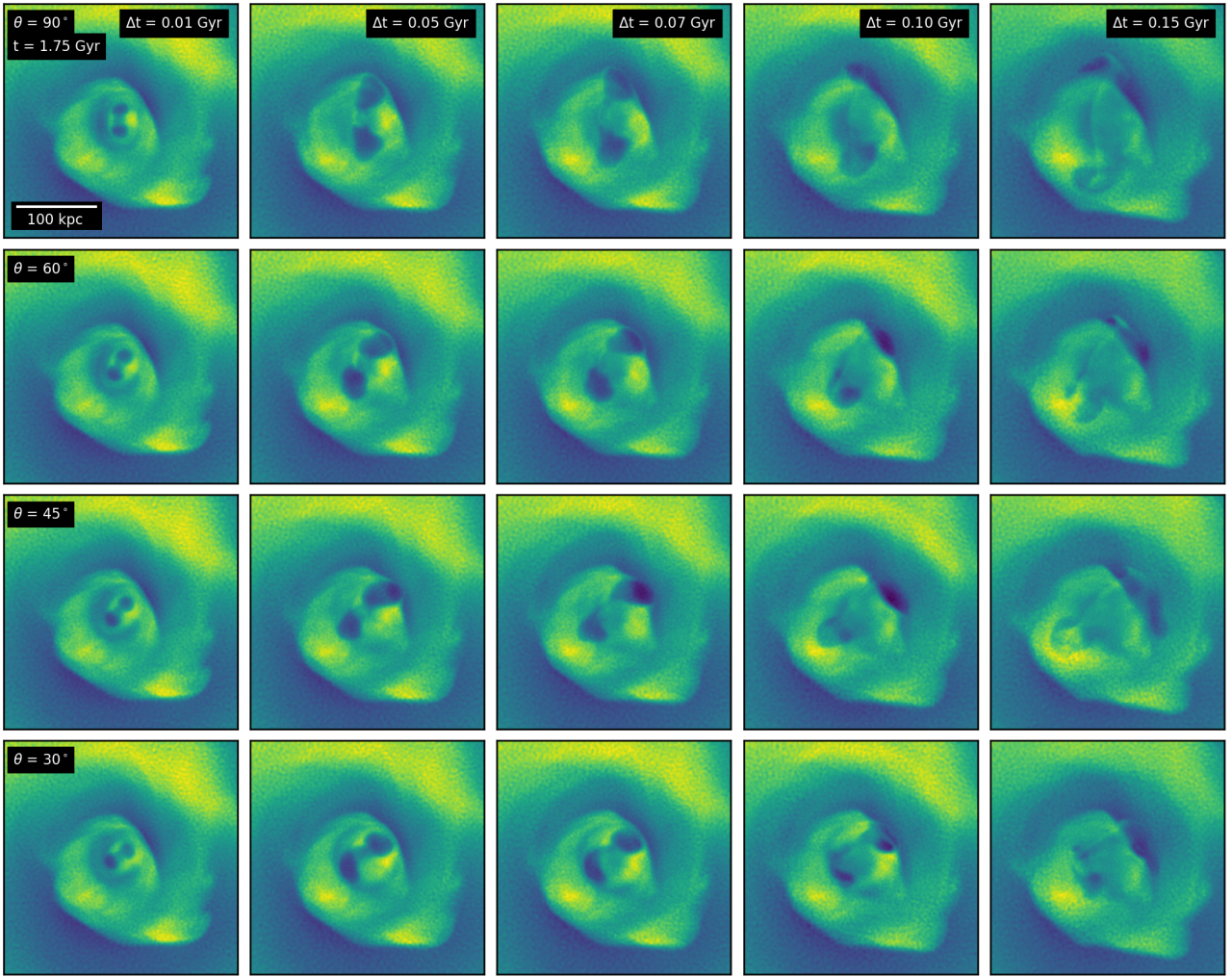


Figure A9. X-ray surface brightness residuals of simulation with sloshing gas motions and AGN jets, where the jet axis is 90, 60, 45, and 30 degrees from the horizontal. Epochs shown are $\Delta t = 0.01, 0.05, 0.07, 0.1,$ and 0.15 Gyr from the jet ignition at $t = 1.75$ Gyr.

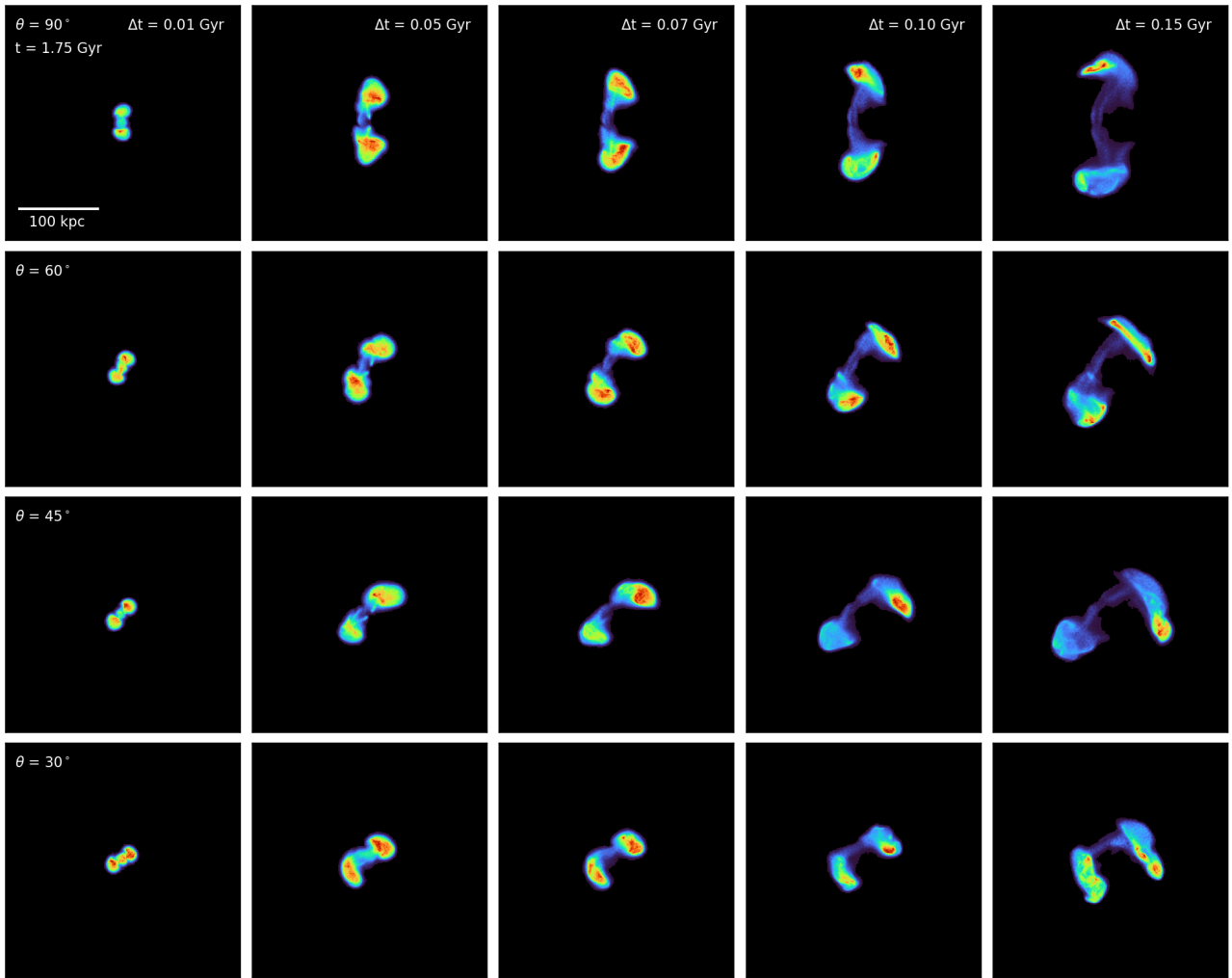


Figure A10. Projected CR energy density of simulation with sloshing gas motions and AGN jets, where the jet axis is 90, 60, 45, and 30 degrees from the horizontal. Epochs shown are $\Delta t = 0.01, 0.05, 0.07, 0.1,$ and 0.15 Gyr from the jet ignition at $t = 1.75$ Gyr.

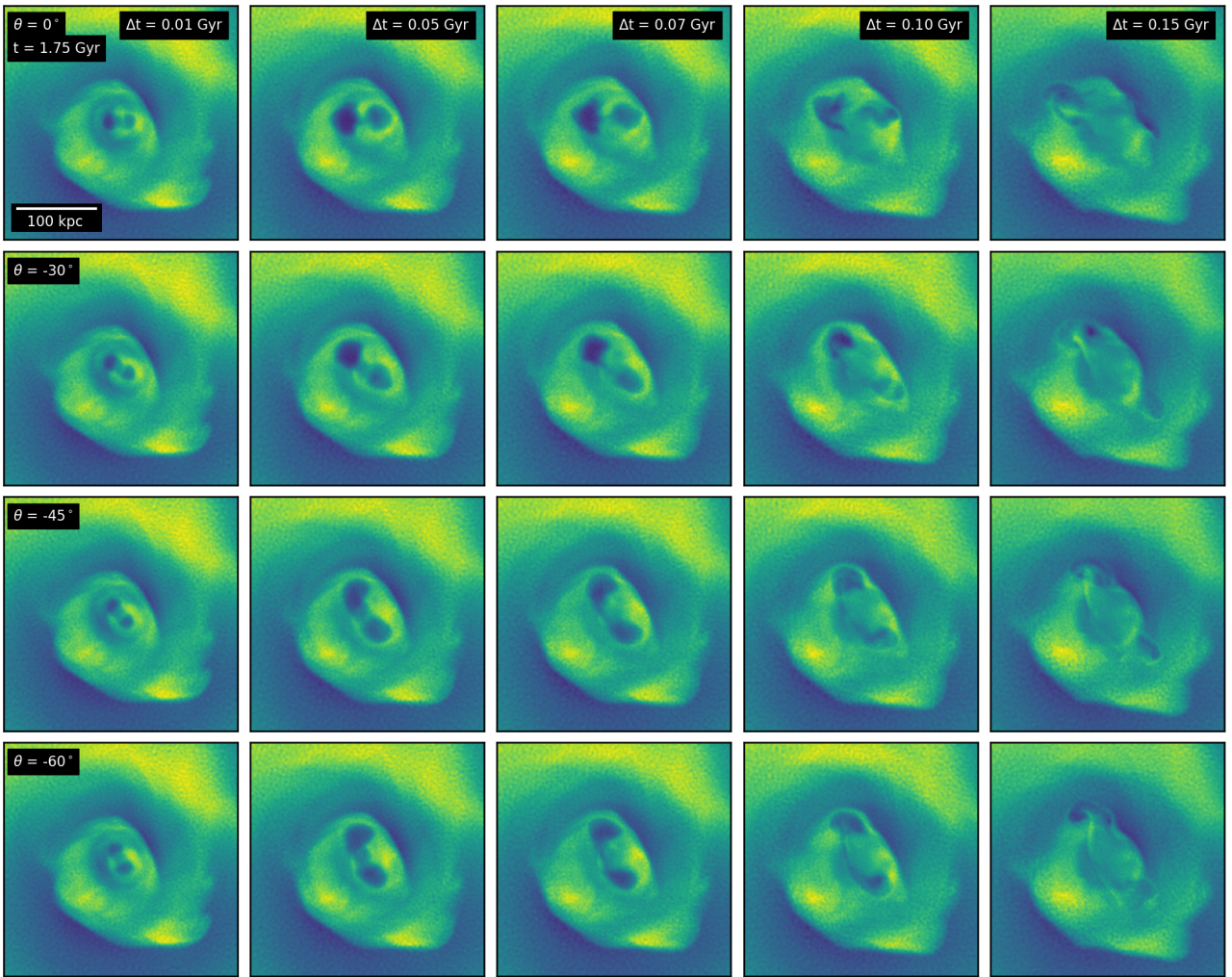


Figure A11. X-ray surface brightness residuals of simulation with sloshing gas motions and AGN jets, where the jet axis is 0, -30, -45, and -60 degrees from the horizontal. Epochs shown are $\Delta t = 0.01, 0.05, 0.07, 0.1,$ and 0.15 Gyr from the jet ignition at $t = 1.75$ Gyr.

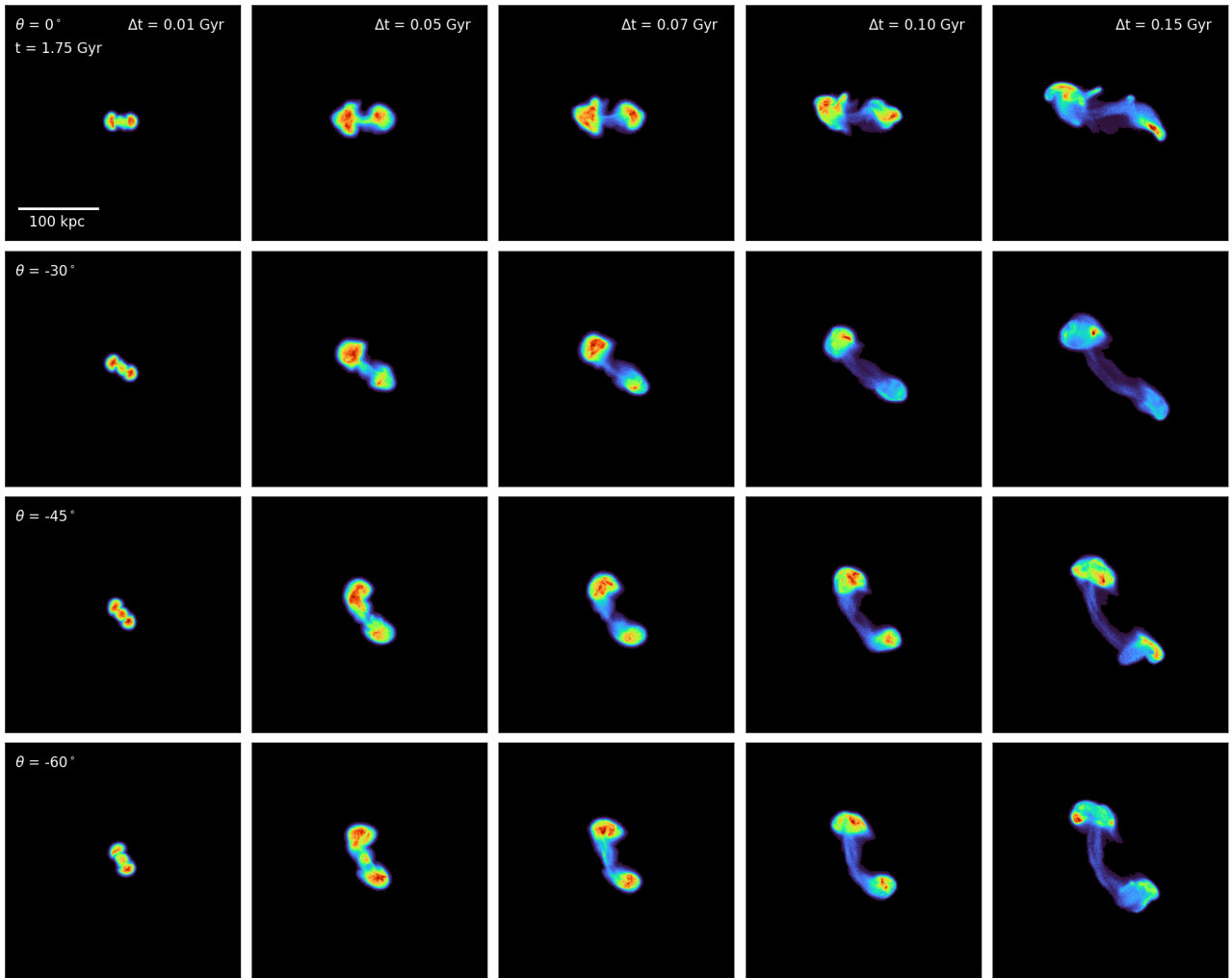


Figure A12. Projected CR energy density of simulation with sloshing gas motions and AGN jets, where the jet axis is 0, -30, -45, and -60 degrees from the horizontal. Epochs shown are $\Delta t = 0.01, 0.05, 0.07, 0.1,$ and 0.15 Gyr from the jet ignition at $t = 1.75$ Gyr.